

Scaling relations between black holes and their host galaxies: comparing theoretical and observational measurements, and the impact of selection effects

C. DeGraf^[1,2] T. Di Matteo^[2], T. Treu^[3,4], Y. Feng^[2], J.-H. Woo^[5], D. Park^[6]

¹ Center for Astrophysics and Planetary Science, Racah Institute of Physics, The Hebrew University, Jerusalem 91904, Israel

² McWilliams Center for Cosmology, Carnegie Mellon University, 5000 Forbes Avenue, Pittsburgh, PA 15213, USA

³ Department of Physics, University of California, Santa Barbara, CA 93106, USA

⁴ Department of Physics and Astronomy, University of California, Los Angeles, CA 90095

⁵ Astronomy Program, Department of Physics and Astronomy, Seoul National University, Seoul, 151-742, Republic of Korea

⁶ National Astronomical Observatories, Chinese Academy of Sciences, Beijing 100012, China; EACOA fellow

Submitted to MNRAS

ABSTRACT

We use the high-resolution simulation *MassiveBlackII* to examine scaling relations between supermassive black hole mass (M_{BH}) and their host galaxies' properties (σ , total M_* and L_V), finding good agreement with recent observational data, especially at the high-mass end. The simulations have less intrinsic scatter than observations, and the $M_{\text{BH}} - L_V$ correlation has the largest scatter, suggesting it may be the least fundamental of the three relations. We find Gaussian scatter about all three relations, except among the highest mass galaxies, which host more massive black holes. Below $z \sim 2$ the slopes for the full population remain roughly z -independent, and only steepen by 50% by $z \sim 4$. The normalization of the σ , L_V relations evolve by 0.3, 0.43 dex, while the M_{BH} correlation does not evolve out to at least $z \sim 2$. Testing for selection biases, we find samples selected by M_{BH} or M_* have steeper slopes than randomly selected samples. If unaccounted for, such a selection function would find faster evolution than inferred from a randomly selected sample, as objects at the high-end of the relation tend to evolve more rapidly. We find a potential bias among high- L_{BH} subsamples (tending to reside in higher mass galaxies), but these bright-AGN exhibit no intrinsic bias relative to fainter ones in equivalent-mass hosts, nor is there a significant difference between active- and inactive- samples. Finally we characterize the evolution of individual black holes along the scaling planes. Below the local relation, black holes grow faster than their host (72% of black holes > 0.3 dex below the mean relation have a $M_{\text{BH}} - M_*$ trajectory steeper than the local relation), while those above have shallower trajectories (only 14% are steeper than local). Thus black holes tend to grow faster than their hosts until surpassing the local relation, at which point their growth is suppressed while their hosts continue to grow, returning them to the mean relation.

Key words: quasars: general — galaxies: active — black hole physics — methods: numerical — galaxies: haloes

1 INTRODUCTION

In the local universe, the discovery of close relationships between the masses of supermassive black holes and several properties of their bulges such as the stellar mass (Magorrian et al. 1998; Häring & Rix 2004), stellar velocity dispersion ($M_{\text{BH}} - \sigma$ relation, Gebhardt et al. (2000); Ferrarese (2002); Tremaine et al. (2002); Ferrarese (2002); Gültekin et al. (2009); McConnell et al. (2011); McConnell & Ma (2013), and the concentration param-

eter (Graham et al. 2001) have revolutionized our view of BHs, linking their growth to that of its host galaxy (for a recent review see also Kormendy & Ho 2013). Most recently, McConnell & Ma (2013) have re-analyzed the scaling relations and added a number of high mass objects. To understand the evolution of these relations at higher redshifts (mostly up to $z \sim 2$) observational studies rely on galaxies with active galactic nuclei (Merloni et al. 2010; Bennert et al. 2010, 2011b,a; Kormendy & Ho 2013; Park et al. 2014) for which BH mass estimates use the so-

called virial method (Wandel et al. 1999). Whereas some studies have found an evolution in which BH growth precedes that of their host galaxies, others found no evolution within the uncertainties. These observations are challenging and their interpretation relies on a full understanding of systematic uncertainties (in both the BH mass and host galaxy measurements, e.g. Woo et al. 2006) and selection effects (Treu et al. 2007; Lauer et al. 2007; Schulze & Wisotzki 2011, 2014). Without a proper modeling of the uncertainties, selection effects at high redshift can lead to much stronger apparent evolution than the true population undergoes, and underestimate the slope of the relations (Volonteri & Stark 2011).

A popular way to interpret these relationships is by assuming that supermassive BHs regulate their own growth and that of their hosts by coupling some (small) fraction of their energy output to their surrounding gas. This, so called, “AGN feedback” heats and unbinds significant fractions of the gas and inhibits star formation (Silk & Rees 1998; Springel et al. 2005; Bower et al. 2006; Croton et al. 2006; Di Matteo et al. 2008; Ciotti et al. 2009; Fanidakis et al. 2011). The scaling relations of black hole mass with the stellar properties of the host galaxies have important implications for black hole and galaxies as well as understanding the importance and the effects of AGN feedback.

Here we use state-of-the-art cosmological hydrodynamical simulations of structure formation (*MassiveBlack-II*) (Khandai et al. 2014) to investigate the predictions of the galaxy-black hole relations $M_{\text{BH}} - \sigma$, $M_{\text{BH}} - M_{*,\text{tot}}$ and $M_{\text{BH}} - L_{V,\text{tot}}$ relations for the population of black holes and compare them to the observational constraints at $z = 0 - 2$. MBII is a recent large-scale and high resolution hydrodynamic simulation in a box of 100Mpc/h on the side, making one of the largest cosmological Smooth Particle Hydrodynamics (SPH) simulation to date with full physics of galaxy formation (meaning here an inclusion of radiative cooling, star formation, black hole growth and associated feedback physics). Note that Sijacki et al. (2014) has also presented results on the black hole scaling relations from the Illustris moving-mesh simulation (Vogelsberger et al. 2014), also well matching the local relation and finding significant redshift evolution.

We concentrate on the prediction for the black hole-galaxy relations relative to the the *total* stellar mass and luminosity of the host galaxy as measured by Merloni et al. (2010); Bennert et al. (2010, 2011b,a); Kormendy & Ho (2013); Park et al. (2014). The predictions from the simulations are most direct for the total quantities (stellar mass and luminosity) and we do not need to introduce unknown biases as we would have if we used proxies for these measurements in galaxy bulge components (we reserve this work to a future analysis with morphological decomposition). The aim is then to first clearly understand these different relations (e.g. which one may be the strongest correlation), as well as predict the expected redshift evolution for $M_{\text{BH}} - M_{*,\text{tot}}$ and $M_{\text{BH}} - L_{V,\text{tot}}$ planes. We will also address the issue of selection effects in observing these relations. Since the observational investigations into scaling relations at $z > 0$ use AGN-selected samples with luminosity limitations, understanding the effect L_{BH} and M_{BH} has on the scaling relations is also significant.

The paper is organized as follows: In Section 2 we will

briefly describe MBII simulation and the black hole model contained therein. In Section 3 we investigate the 3 primary scaling relations and their redshift evolution (§3.1 and 3.2), the dependence on black hole luminosity (§4.1) and the evolution of typical black hole mass (§3.3). In Section 4 we discuss how the distribution of objects in smaller subsamples selected by M_* or M_{BH} can bias the inferred slope and evolution of the scaling relations, and in Section 5 we probe the typical evolution of individual black holes on the scaling relation planes. We summarize our results in Section 6.

2 METHOD

In this paper we use a cosmological hydrodynamic simulation *MassiveBlackII* (Khandai et al. 2014). This simulation is similar (in terms of the physics modelled) to the high-redshift 533 h^{-1} Mpc *MassiveBlack* simulation, using a smaller (100 h^{-1} Mpc) box, but allowing for higher-resolution and a complete run to $z \sim 0$ (see Table 1). These simulations have been performed with the cosmological TreePM-Smooth Particle Hydrodynamics (SPH) code P-GADGET, a *hybrid* version of the parallel code GADGET2 (Springel 2005) which has been extensively modified and upgraded to run on the new generation of Petaflop scale supercomputers. The major improvement over previous versions of GADGET is in the use of threads in both the gravity and SPH part of the code which allows the effective use of multi core processors combined with an optimum number of MPI task per node. The *MassiveBlackII* simulation contains $N_{\text{part}} = 2 \times 1792^3 = 11.5$ billion particles in a volume of 100Mpc/h on a side with a gravitational smoothing length $\epsilon = 2.0\text{kpc/h}$ (in comoving units). The gas and dark matter particle masses are $m_g = 2.1 \times 10^6 M_\odot$ and $m_{\text{DM}} = 1 \times 10^7 M_\odot$ respectively. The simulation has currently been run from $z = 159$ to $z = 0.06$.

The run contains the standard gravity and hydrodynamics, as well as additional (subgrid) modeling for star formation (Springel & Hernquist 2003), black holes and associated feedback processes (Di Matteo et al. 2008, 2012). The cosmological parameters used were: the amplitude of mass fluctuations, $\sigma_8 = 0.8$, spectral index, $n_s = 0.96$, cosmological constant parameter $\Omega_\Lambda = 0.725$, mass density parameter $\Omega_m = 0.275$, baryon density parameter $\Omega_b = 0.044$ and $h = 0.702$ (Hubble’s constant in units of $100\text{km s}^{-1}\text{Mpc}^{-1}$), based on WMAP7.

Within our simulation, black holes are modeled as collisionless sink particles which form in newly emerging and resolved dark matter halos. These halos are found by calling a friends of friends group finder at regular intervals (in time intervals spaced by $\Delta \log a = \log 1.25$). Any group above a threshold mass of $5 \times 10^{10} h^{-1} M_\odot$ not already containing a black hole is provided one by converting its densest particle to a sink particle with a seed mass of $M_{\text{BH,seed}} = 5 \times 10^6 h^{-1} M_\odot$. This seeding prescription is chosen to reasonably match the expected formation of supermassive black holes by gas directly collapsing to BHs with $M_{\text{BH}} \sim M_{\text{seed}}$ (e.g. Bromm & Loeb 2003; Begelman et al. 2006) or by PopIII stars collapsing to $\sim 10^2 M_\odot$ BHs at $z \sim 30$ (Bromm & Larson 2004; Yoshida et al. 2006) followed by sufficient exponential growth to reach M_{seed} by the time the host halo reaches $\sim 10^{10} M_\odot$. Following in-

Table 1. Numerical Parameters for the *MassiveBlackII* simulation

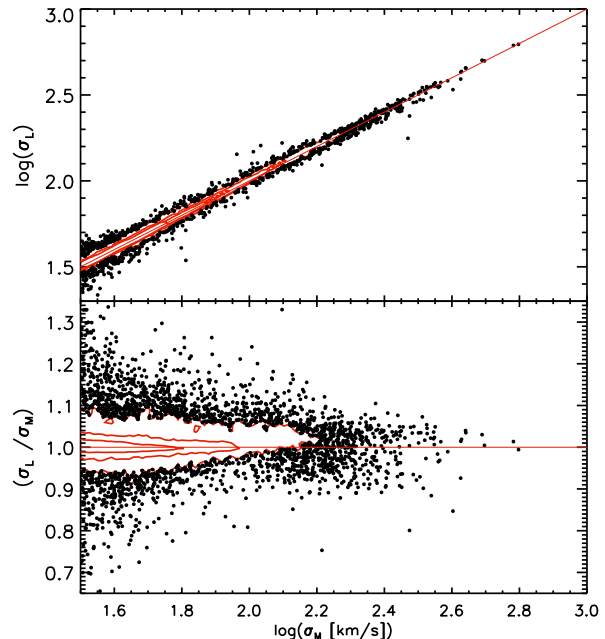
Boxsize h^{-1} Mpc	N_p	m_{DM} $h^{-1}M_\odot$	m_{gas} $h^{-1}M_\odot$	ϵ h^{-1} kpc
100	2×1792^3	1×10^7	2.1×10^6	2.0

section, BHs grow in mass by accretion of surrounding gas and by merging with other black holes. Gas is accreted according to $\dot{M}_{BH} = \alpha \frac{4\pi G^2 M_{BH}^2 \rho}{(c_s^2 + v^2)^{3/2}}$ (Hoyle & Lyttleton 1939; Bondi & Hoyle 1944; Bondi 1952), where ρ is the local gas density, c_s is the local sound speed, v is the velocity of the BH relative to the surrounding gas, and α is introduced to correct for the reduction of the gas density close to the BH due to our effective sub-resolution model for the ISM. To allow for the initial rapid BH growth necessary to produce sufficiently massive BHs at early time ($\sim 10^9 M_\odot$ by $z \sim 6$) we allow for mildly super-Eddington accretion (consistent with Volonteri & Rees 2006; Begelman et al. 2006), but limit it to a maximum of $3 \times \dot{M}_{Edd}$ to prevent artificially high values.

The BH is assumed to radiate with a bolometric luminosity proportional to the accretion rate, $L = \eta \dot{M}_{BH} c^2$ (Shakura & Sunyaev 1973), where the radiative efficiency η is fixed to 0.1 throughout the simulation and our analysis. To model the expected coupling between the liberated radiation and the surrounding gas, 5 per cent of the luminosity is isotropically deposited to the local black hole kernel as thermal energy. The 5 per cent value for the coupling factor is based on galaxy merger simulations such that the normalization of the $M_{BH} - \sigma$ relation is reproduced (Di Matteo et al. 2005).

The second mode of black hole growth is through mergers which occur when dark matter halos merge into a single halo, such that their black holes fall toward the center of the new halo, eventually merging with one another. In cosmological volumes, it is not possible to directly model the physics of the infalling BHs at the smallest scales, so a sub-resolution model is used. Since the mergers typically occur at the center of a galaxy (i.e. a gas-rich environment), we assume the final coalescence will be rapid (Makino & Funato 2004; Escala et al. 2004; Mayer et al. 2007), so we merge the BHs once they are within the spatial resolution of the simulation. However, to prevent merging of BHs which are rapidly passing one another, mergers are prevented if the BHs' velocity relative to one another is too high (comparable to the local sound speed).

The model used for black hole creation, accretion and feedback has been investigated and discussed in Sijacki et al. (2007); Di Matteo et al. (2008); Colberg & di Matteo (2008); Croft et al. (2009); Sijacki et al. (2009); DeGraf et al. (2010); Degraf et al. (2011), finding it does a good job reproducing the $M_{BH} - \sigma$ relation, the total black hole mass density (Di Matteo et al. 2008), the QLF (DeGraf et al. 2010), and the expected black hole clustering behavior (Degraf et al. 2011). This simple model thus appears to model the growth, activity, and evolution of supermassive black holes in a cosmological context surprisingly well (though the detailed treatment of the accretion physics is infeasible for cosmological scale

**Figure 1.** Direct comparison between velocity dispersion within half-mass radius (σ_M) and within half-light radius (σ_L). Top panel shows direct comparison between the two dispersions; bottom panel shows the ratio σ_L/σ_M as a function of σ_M .

simulations). We also note that Booth & Schaye (2009) and Johansson et al. (2008) have adopted a very similar model, and have independently investigated the parameter space of the reference model of Di Matteo et al. (2008), as well as varying some of the underlying prescriptions. For further details on the simulation methods and convergence studies done for similar simulations, see Di Matteo et al. (2008).

Because the simulation saves the complete set of black hole properties (mass, accretion rate, position, local gas density, sound speed, velocity, and BH velocity relative to local gas) for each BH at every timestep, the black hole output for such a large simulation is prohibitively difficult to analyze using previous techniques. For this reason, Lopez et al. (2011) developed a relational database management system specifically for this simulation. A similar strategy has also been followed in the analysis of the Millenium simulation (Lemson & Virgo Consortium 2006). In addition to providing a substantially more efficient query system for extracting information, this database is significantly more flexible than traditional approaches. For a complete summary of the database format and its efficiency, please see Lopez et al. (2011).

Catalogues of galaxies are made from the simulation outputs by first using a friends-of-friends groupfinder and then applying the SUBFIND algorithm (Springel 2001) to find gravitationally bound subhalos. The stellar component of each subhalo consists of a number of star particles, each labelled with a mass and the redshift at which the star particle was created.

For our galaxies the spectral energy distribution (SED) of a galaxy is generated by summing the SEDs of each star particle in the galaxy. The SED of the star particles is gen-

erated using the Pegase.2 stellar population synthesis (SPS) code (Fioc & Rocca-Volmerange 1997, 1999) by considering their ages, mass and metallicities and assuming a Salpeter IMF. Nebula (continuum and line) emission is also added to each star. With stellar luminosity we have information about direct half-light radii of galaxies and can carry out a luminosity-weighted velocity dispersion for our subgroups catalog. To most closely match observational studies, for this work we use the V-band rest frame as our luminosity band.

3 THE SCALING RELATIONS

3.1 $M_{\text{BH}} - \sigma$

Figure 1 compares σ_L , the velocity dispersion within the half-light radius, to σ_M , within the half-mass radius (a proxy commonly adopted in simulation for the bulge velocity dispersion). Although there is noticeable scatter between the two calculations, there is no systematic offset between σ_L and σ_M (even at lower- σ the scatter remains $\sim 20\%$). This lack of a systematic offset suggests that either proxy is adequate given the scatter of the relations; however we caution that possible residual systematics at the 20% level might be present (as mass and light trace each other at these scales). Furthermore, this proxy neglects the addition of rotational velocity, and is more uncertain at the low mass end (Sijacki et al. (see 2014)). This precise impact is investigated in detail in an upcoming paper on bulge-decomposition in the simulation (Tenneti 2014). For the rest of this analysis we choose to work with σ_L , since the luminosity-radius is more similar to observational approaches. Note that for the remainder of this paper we refer only to σ (with no subscript), but in all cases it is used to refer to the V-band luminosity-weighted velocity dispersion within the V-band half-light radius.

In Figure 2 we show the $M_{\text{BH}} - \sigma$ relation from our simulation in the redshift range 0.06-4. These results are shown as black datapoints, with red contours representing the regions of highest concentration (to show the behavior where the concentration of points is too high). Note that we only consider central black holes (see also Sijacki et al. 2014). Observational data from Woo et al. (2006, 2008); Bennert et al. (2011b); McConnell & Ma (2013); Kormendy & Ho (2013) are shown as colored points. We also provide a best-fitting relation for our black holes (dashed pink line). For reference, the best-fitting relation from the $z=0.06$ panel is shown in all panels as a solid grey line. The best-fitting lines are calculated using the functional form

$$\frac{M_{\text{BH}}}{M_{\odot}} = 10^{\alpha} \left(\frac{x}{x_0} \right)^{\beta} \quad (1)$$

(where $x = \sigma, M_*, L_V$, etc.). Following McConnell & Ma (2013), this fitting is accomplished using the least-squares fitting routine MPFITEXY (see Williams et al. 2010). Each black hole has an uncertainty in σ (ϵ_{σ} , set to the standard deviation of the logarithm of the projected dispersion for the three orthogonal directions). M_{BH} , M_* , and L_V do not have equivalent variations to use, so a 5% uncertainty is assigned to each (though the fits are not sensitive to this value). To avoid the fit being dominated by the low-mass objects (which are less well-resolved and more dependent on the BH seeding prescription), we limit our fits to black

holes within hosts with $M_* > 10^{10} M_{\odot}$ (where M_* is the total stellar mass). The parameters α and β for these fits are provided in Table 2. Following Gültekin et al. (2009) and McConnell & Ma (2013) we include a measure of the intrinsic scatter (ϵ_0), such that

$$\chi^2 = \sum_i \frac{(\log_{10}(M) - \alpha - \beta \log_{10}(\sigma_i/200 \text{ km/s}))^2}{\epsilon_0^2 + \epsilon_{M_{\text{BH},i}}^2 + \beta^2 \epsilon_{\sigma,i}^2} \quad (2)$$

equals the number of degrees of freedom. This intrinsic scatter presents an important component of any scaling analysis, and must be considered when performing the fitting.

When comparing with observational data, we find that our simulation does an excellent job matching the observational data at the high-end (above $\sim 10^{7.3} M_{\odot}$), including the scatter within the relation. At lower-masses and correspondingly low σ (at least at $z = 0$, where such low-mass objects have been observed), our simulations either somewhat overestimate the mass of the black holes in a given galaxy or underestimate σ . Note also that Sijacki et al. (2014) has shown that the effect of adding the rotational velocity component (as typically included in observations) to σ has a strong effect at this end of the relation. In particular, they found that the hosts of low-mass black holes can have a significant rotational component, leading to a larger σ than when using a pure velocity dispersion and bringing our results closer to the observed data. This effect will be investigated in an upcoming work (involving a complete bulge decomposition), but given that we will concentrate on the relations with the total M_* and L_V rather than bulge proxies (see Section 3.2) in this analysis, we will not further need to consider these effects here.

Of particular interest from our simulation is the redshift evolution of the relation, as we have far larger samples and dynamic range at high- z than can be expected from any current observational study. Of particular note in our simulation is that the $M_{\text{BH}} - \sigma$ relation has minimal evolution out to $z \sim 1$, with the slope changing by less than 10% (similar to the findings of the Magneticum Pathfinder Simulation, Hirschmann et al. 2014; Bachmann et al. 2014), and the normalization by only 0.2 dex (see also Section 4). At $z = 2 - 4$ we find somewhat more evolution, with the typical black hole mass being smaller, and the slope being steeper. This is consistent with the ‘selective accretion’ prediction of Volonteri & Stark (2011), that accretion is more efficient in high-mass halos at high redshift, while at low redshift baryonic processes wash out this dependence on halo mass. However, we note that this is due, at least in part, to the more-recently seeded black holes. Particularly at $z = 4$, we see that in the low- σ hosts (below $\sigma \sim 100$ km/s), the relation begins to flatten close to $10^6 M_{\odot}$, where we are close to our seed mass.

3.2 $M_{\text{BH}} - M_*$ and $M_{\text{BH}} - L_V$

In Figures 3 and 4 we show the $M_{\text{BH}} - M_*$ and $M_{\text{BH}} - L_V$ relations, respectively. We calculate the stellar mass (M_*) and V-band luminosity (L_V) within 2 times the V-band half-light radius (this definition does not differ from the total in low/intermediate mass systems but it allows us to adequately exclude some of the intracluster light for the massive systems, Vogelsberger et al. (see also 2014)). As in

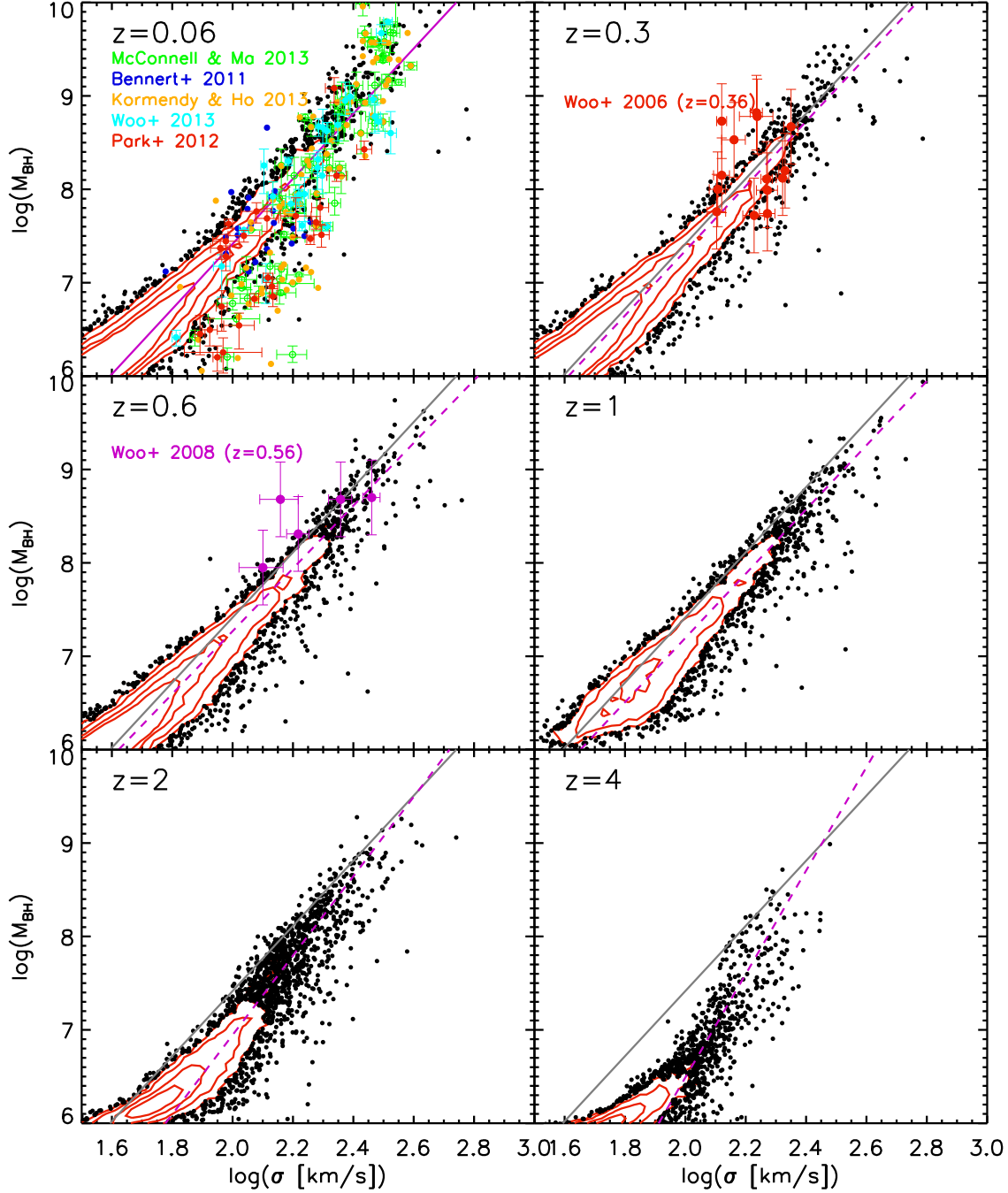


Figure 2. Black hole mass vs. luminosity-weighted stellar velocity dispersion within the half-light radius (black datapoints and red contours). The grey line shows the best-fitting relation calculated at $z = 0.06$, and is included at all redshifts for reference. Observational data are provided as colored datapoints. Note: for the Woo et al. (2006, 2008) data, we use the updated BH mass estimates from Park et al. (2014).

Figure 2, we provide the best fitting relation as a dashed pink line (with the $z = 0.06$ fit shown in all panels in grey for reference), and observational measurements as colored datapoints. When considering current observational measurements for the total relation the agreement is very good with the simulations at $z = 0$. However the scatter in observations is large whilst simulations predict a rather tight relation, with our intrinsic scatter approximately half

that of McConnell & Ma (2013) (note other simulations have also found a tighter correlation than observations, e.g. Ragone-Figueroa et al. 2013). We find a well-defined relation with small scatter ($\epsilon_0 \sim 0.18$), minimal evolution out to redshift 1, and at $z = 2, 4$ the relation is found to be progressively steeper. We note however that Bennert et al. (2011b); Merloni et al. (2010) appear to find a large population of high- M_{BH} , moderate- M_* objects which are offset

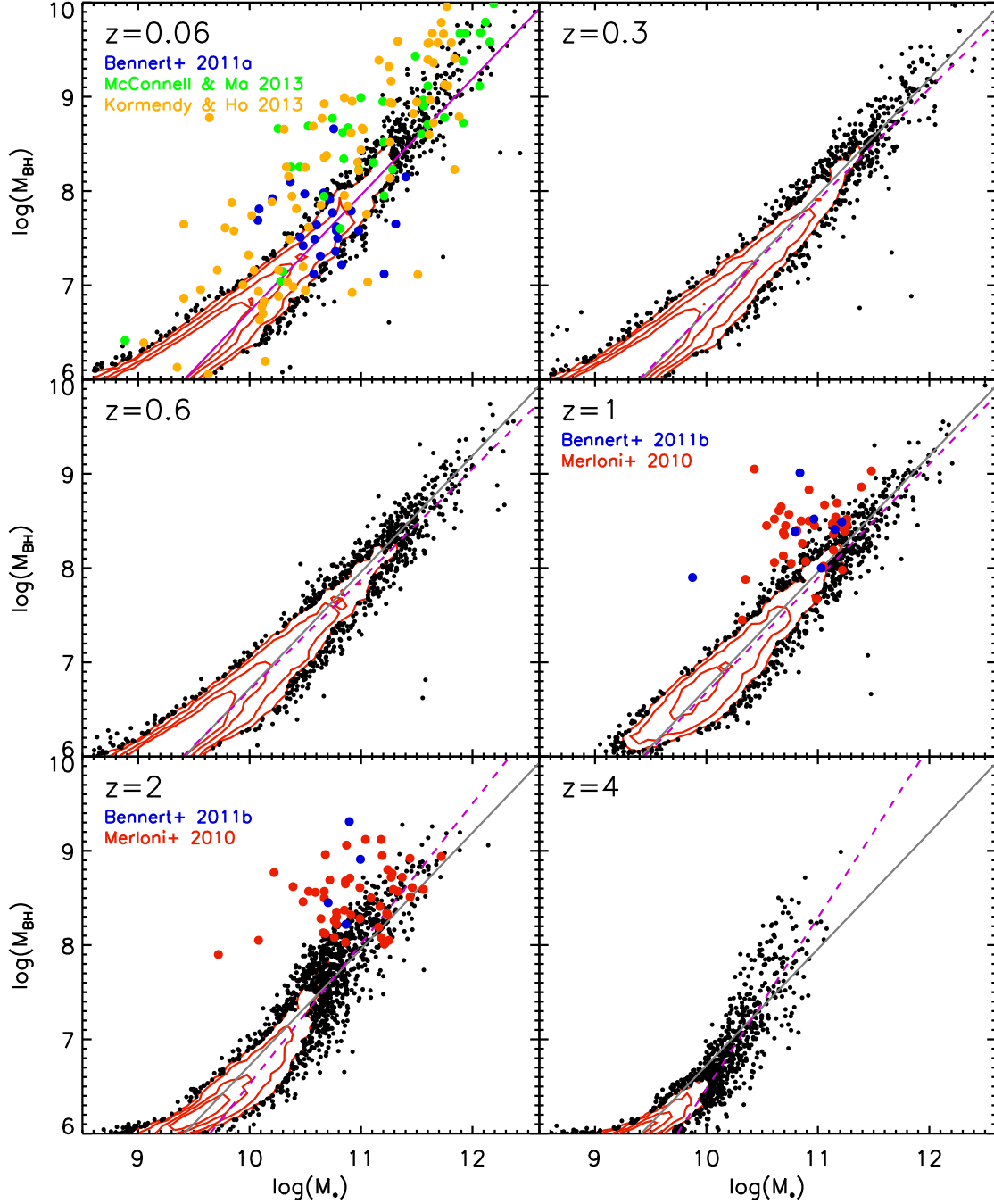


Figure 3. Black hole mass vs. stellar mass within the 2 times the V-band half-light radius (black datapoints and red contours) compared to observational data (colored datapoints). The grey line shows the best-fitting relation calculated at $z = 0.06$, and is included at all redshifts for reference. Note that the data from McConnell & Ma (2013) and Kormendy & Ho (2013) are bulge mass, not total mass, and should thus be considered lower-limits for the M_* comparison.

from the simulation relation, particularly at $z = 1$ and 2. The disagreement at these redshifts could be due to an unaccounted for selection bias in the observations (biasing the results toward higher-mass black holes), systematic uncertainties in the virial black hole measurements at these redshifts, or a problem with the simulation underproducing sufficiently large black holes at $z \sim 1$ and above. This is somewhat hard to envisage as it would require a some population of black

holes which are capable of growing almost 2 dex above the local relation without reaching a self-regulating phase that slows the BH growth (in sharp contrast to the evolution we find in Section 5). We note that at $z = 0.06$, the data from McConnell & Ma (2013) and Kormendy & Ho (2013) both have a population that lies above our black holes, contributing to the much larger scatter in the observations than in the simulations. This high-mass population is due, at least

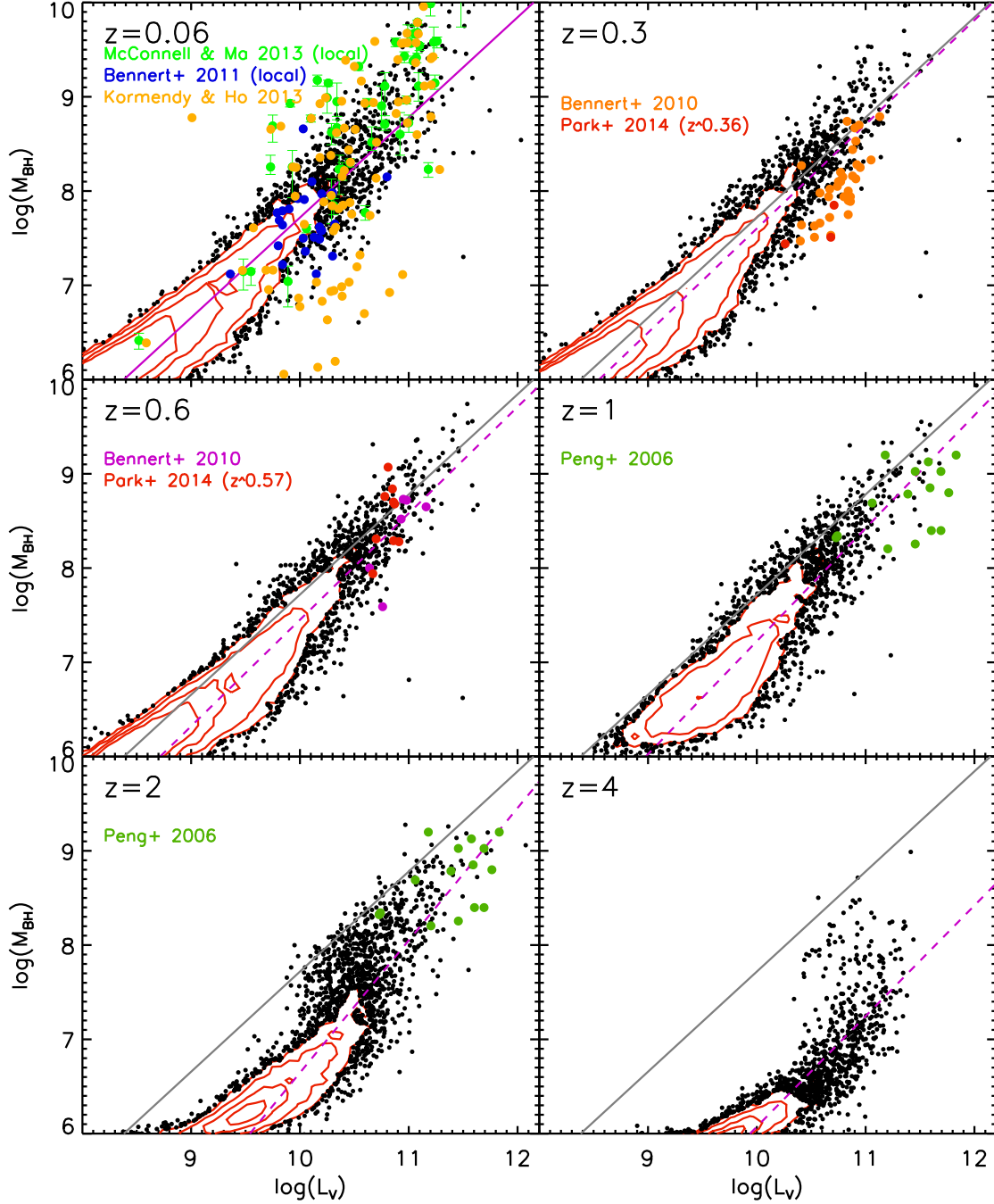


Figure 4. Black hole mass vs. observed V-band luminosity within 2 times the half-light radius (black datapoints and red contours) compared to observational data (colored datapoints). The grey line shows the best-fitting relation calculated at $z = 0.06$, and is included at all redshifts for reference.

in part, to the fact that both McConnell & Ma (2013) and Kormendy & Ho (2013) use the stellar mass of the bulge (for both elliptical and spiral galaxies), rather than the full stellar mass we use. In particular, we note that the low-mass objects from Kormendy & Ho (2013) where we have the strongest discrepancy are the spiral and S0 type galaxies (where the bulge mass is a significant underestimate), while the high-mass objects are ellipticals, suggesting that correcting for the total mass may help solve this discrepancy.

This will be investigated in more detail in an upcoming work involving a complete bulge-decomposition (Tenneti 2014). The second difference from Figure 2 is that the evolution of the relation to $z = 2, 4$ is notably different than that of $M_{\text{BH}} - \sigma$. Unlike the $M_{\text{BH}} - \sigma$ relation, we find that the high-mass objects at $z = 2, 4$ tend to be *larger* with respect to their host mass than a comparable object at lower-redshift, telling us that at high-redshift, the black holes are being fuelled more efficiently (compared to their host galaxy) than

Parameters for scaling relation			
z	α	β	ϵ_0
$M_{\text{BH}} - \sigma$ relation ($x_0 = 200\text{km/s}$)			
0.06	8.465 ± 0.007	3.487 ± 0.019	0.169
0.3	8.317 ± 0.006	3.295 ± 0.019	0.163
0.6	8.206 ± 0.007	3.186 ± 0.020	0.179
1	8.154 ± 0.007	3.248 ± 0.022	0.192
2	8.091 ± 0.011	3.852 ± 0.037	0.235
4	7.860 ± 0.030	4.416 ± 0.137	0.292
$M_{\text{BH}} - M_*$ relation ($x_0 = 10^{11} M_\odot$)			
0.06	7.957 ± 0.004	1.235 ± 0.007	0.184
0.3	7.903 ± 0.004	1.183 ± 0.006	0.175
0.6	7.878 ± 0.004	1.174 ± 0.007	0.179
1	7.891 ± 0.005	1.213 ± 0.008	0.189
2	8.014 ± 0.009	1.486 ± 0.013	0.231
4	8.290 ± 0.040	1.815 ± 0.053	0.291
$M_{\text{BH}} - L_V$ relation ($x_0 = 10^{10.5} L_\odot$)			
0.06	8.249 ± 0.008	1.062 ± 0.008	0.258
0.3	8.155 ± 0.008	1.106 ± 0.009	0.256
0.6	8.016 ± 0.008	1.129 ± 0.010	0.264
1	7.823 ± 0.008	1.198 ± 0.013	0.285
2	7.347 ± 0.008	1.404 ± 0.022	0.352
4	6.659 ± 0.031	1.174 ± 0.086	0.450

Table 2. Best fitting parameters for the scaling relations (Equation 1).

a similar object at low-redshift. This is consistent with previous high-redshift growth rates found in these simulations (DeGraf et al. 2012).

Finally, Figure 4 shows the BH mass relative to the host luminosity. Here we note several important differences with respect to the previous relations. Firstly, the $M_{\text{BH}} - L_V$ relation has an intrinsic scatter approximately 50% larger than either $M_{\text{BH}} - \sigma$ or $M_{\text{BH}} - M_*$, consistent at all redshifts, suggesting that the relation with σ and with M_* are more fundamental than L_V . This is consistent with the findings of McConnell & Ma (2013); Kormendy & Ho (2013). Secondly, we find significantly more evolution in the typical black hole mass for a given host luminosity. Rather than an inherent change in the BH-host relation, this can be interpreted as an evolution in the typical mass-to-light ratio of the host galaxy, since high- z galaxies tend to host younger, and therefore brighter, stellar populations. This effect is discussed in more detail (including using an evolution-corrected luminosity $L_{V,0}$) in Section 3.3 while investigating evolution of the typical black hole mass.

3.3 Redshift evolution of BH-galaxy relations

To provide an accurate estimate for the evolution of a typical black hole relative to its host, in the top panel of Figure 5 we show the average mass offset ($\Delta(M_{\text{BH}})$) relative to our best-fitting local $M_{\text{BH}} - M_*$ relation (i.e. using the $z = 0.06$ best-fitting parameters from Table 2). Due to the large number of black holes in our simulation, we do not show individual objects, but rather the average offset, with $1 - \sigma$ scatter provided. We provide four such curves, using four different lower-limits on black hole mass. To avoid recently-seeded

Dependency on L_{BH} , σ , M_*			
	α	β	ϵ_0
$M_{\text{BH}} - \sigma$ relation ($x_0 = 200\text{km/s}$)			
$L_{\text{BH}} > 10^8 L_\odot$	8.467 ± 0.007	3.447 ± 0.019	0.158
$L_{\text{BH}} > 10^9 L_\odot$	8.518 ± 0.009	3.520 ± 0.034	0.188
$L_{\text{BH}} > 10^{10} L_\odot$	8.636 ± 0.013	3.765 ± 0.079	0.204
$L_{\text{BH}} > 10^{11} L_\odot$	8.677 ± 0.033	4.135 ± 0.218	0.249
$\sigma < 200\text{km/s}$	8.681 ± 0.042	2.688 ± 0.296	0.351
$\sigma > 200\text{km/s}$	8.415 ± 0.008	3.354 ± 0.022	0.155
$M_* < 10^{10.5} M_\odot$	8.286 ± 0.026	3.038 ± 0.060	0.139
$M_* > 10^{10.5} M_\odot$	8.511 ± 0.009	3.827 ± 0.042	0.199
$M_{\text{BH}} - M_*$ relation ($x_0 = 10^{11} M_\odot$)			
$L_{\text{BH}} > 10^8 L_\odot$	7.965 ± 0.004	1.222 ± 0.007	0.176
$L_{\text{BH}} > 10^{10} L_\odot$	8.093 ± 0.012	1.298 ± 0.024	0.203
$\sigma < 200\text{km/s}$	8.333 ± 0.074	0.878 ± 0.096	0.358
$\sigma > 200\text{km/s}$	7.931 ± 0.005	1.196 ± 0.008	0.171
$M_* < 10^{10.5} M_\odot$	7.824 ± 0.018	1.054 ± 0.022	0.160
$M_* > 10^{10.5} M_\odot$	7.955 ± 0.005	1.345 ± 0.014	0.208
$M_{\text{BH}} - L_V$ relation ($x_0 = 10^{10.5} L_\odot$)			
$L_{\text{BH}} > 10^8 L_\odot$	8.266 ± 0.008	1.055 ± 0.008	0.245
$L_{\text{BH}} > 10^{10} L_\odot$	8.449 ± 0.016	1.116 ± 0.035	0.313
$\sigma < 200\text{km/s}$	8.754 ± 0.046	0.564 ± 0.092	0.397
$\sigma > 200\text{km/s}$	8.155 ± 0.009	0.973 ± 0.009	0.239
$M_* < 10^{10.5} M_\odot$	7.454 ± 0.025	0.400 ± 0.022	0.204
$M_* > 10^{10.5} M_\odot$	8.291 ± 0.010	1.043 ± 0.016	0.288

Table 3. Dependency of the scaling relations (Equation 1) on black hole luminosity, host velocity dispersion, and stellar mass.

objects, our lowest limit is $10^7 M_\odot$, with approximately half-dex intervals up to $3 \times 10^8 M_\odot$. Regardless of the mass cut, we find essentially no evolution to $z \sim 1$. Above redshift 1, we begin to see significant mass-dependence, showing that low-mass black holes don't evolve much, but the high-mass black holes tend to be more massive relative to their host mass than their low-redshift counterparts. This is consistent with Figure 3, where we saw that the high-mass objects at $z = 2, 4$ go above the local relation. As previously mentioned, this can be explained by the faster growth found in high-redshift black holes.

We also compare our offset evolution to data from Bennert et al. (2010, 2011b); Merloni et al. (2010), and the best-fitting relation of Bennert et al. (2011b) (which takes into account the selection function; dashed line). We note that our evolution is somewhat less than the best-fitting result of Bennert et al. (2011b), but lies well within the scatter of the data.

In the bottom panel of Figure 5 we show the evolution in mass-offset relative to the $M_{\text{BH}} - L_V$ relation, rather than $M_{\text{BH}} - M_*$. We note that if we were to use the base L_V to calculate ΔM_{BH} we would find drastically different behavior, with the black holes at higher redshifts tending to be much less-massive relative to their host luminosities. However, this is primarily due to the evolution in host luminos-

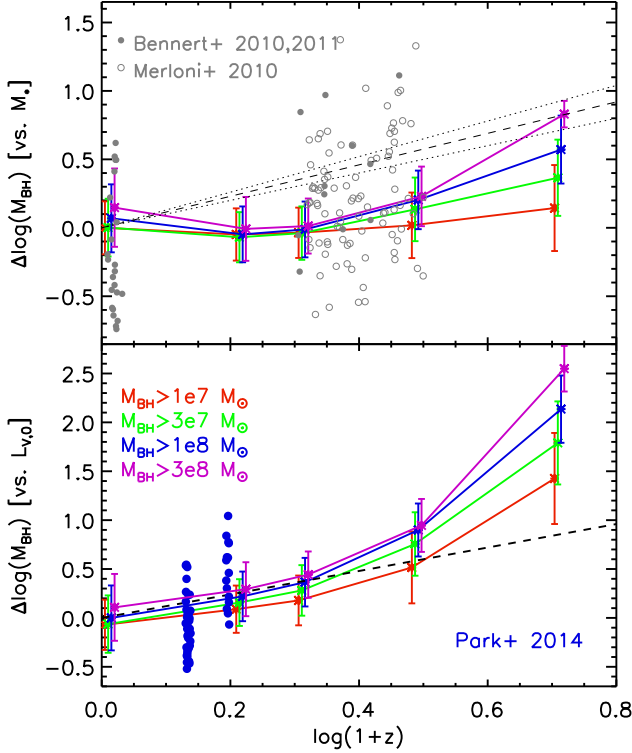


Figure 5. *Top Panel:* M_{BH} offset with respect to our local $M_{\text{BH}} - M_*$ relation as a function of redshift for several cuts on minimum black hole mass. Mass cuts are offset by $\Delta \log(1+z) = 0.005$ to visually separate them. For comparison, we have observational datapoints (Bennert et al. 2010, 2011, Merloni et al. 2011) and the observed best-fit relation (dashed line, with $1-\sigma$ range dotted line) from Bennert et al. 2011. *Bottom Panel:* As in the top panel, but based on the $M_{\text{BH}} - L_V$ relation, using an evolution-corrected value of $L_{V,0}$ (see text). Grey dashed line is the evolution relation from Park et al. (2014).

ity: high- z galaxies host primarily younger stars, and thus tend to be brighter than their low- z counterparts at fixed black hole and stellar mass. Thus the evolution is dominated by the evolution in the stellar-mass-to-light ratio of the host, rather than interactions with the black hole. To account for this, we apply the correction used in Treu et al. (2007), Bennert et al. (2010), and Park et al. (2014): $\log L_{V,0} = \log L_V - (0.62 \pm 0.09) \times z$, and use $L_{V,0}$ when calculating ΔM_{BH} for Figure 5. Having made this correction, ΔM_{BH} relative to host luminosity has a stronger redshift evolution than based on stellar mass. We again note that the evolutionary trend is strongest among high-mass objects, and gets steeper at higher redshifts. To compare directly with observations of Park et al. (2014) we calculate the slope of the evolution for $M_{\text{BH}} > 10^8 M_\odot$ black holes for $z \leq 0.6$, finding a best fit relation of $M_{\text{BH}}/L_{\text{host}} \propto (1+z)^{1.0 \pm 0.1}$, fully consistent with the observational slope of 1.2 ± 0.7 (Park et al. 2014). Given this excellent agreement, we predict that the redshift evolution should get stronger at higher redshifts, which should be investigated in high-redshift surveys.

4 TESTING FOR SAMPLE SELECTION EFFECTS

The large population size of black holes in the simulation allows us to investigate the statistical spread of subsampled populations. To see how the sampling method affects the results, we consider the distribution of best-fit slopes (for all three scaling relations) at $z = 0.06$ and 1, using three different sampling methods with sample sizes of 100 objects. First we consider a random sampling, in which 100 black holes are selected at random from the full population. Then we consider populations uniformly distributed in M_{BH} (M_*), which are made by taking a uniformly-distributed set of 100 masses, ranging from $10^{6.5} M_\odot$ ($10^{10} M_\odot$) to the 15th largest M_{BH} (M_*) in the population, and considering the black hole (host galaxy) with the mass closest to the randomly generated value. For each sampling method, we take 10,000 samples (randomizing the ordering of the full population for each) and find the best fit slope and intrinsic scatter for each sample. To avoid undue contamination from the four strongest outliers (seen in Figure 3), we have removed them from consideration when generating the subsamples (the effect of these outliers is discussed in §4.4). We show the distribution of the best-fitting slopes in Figure 9 and of the intrinsic scatter in Figure 10.

We note several key points from Figure 9. First, the random sample (in red) very closely matches the fit from the full population (black vertical lines), as may be expected. Thus an unbiased sample of black holes will tend to provide an equivalent slope to that of the full population. However, the two samples that use a uniform mass distribution (in blue and green) show significantly steeper slopes. As discussed in Section 4.1, the low-end of the relation tends to be shallower. Since low-mass objects are much more common than high-mass objects, the random sample tends to be more strongly weighted toward the low-end (according to the black hole mass function). However, by selecting uniformly by M_{BH} or M_* we weight all mass-scales equally. With relatively less weight on the low-end, the resulting slope tends to be steeper. This sampling bias is stronger at $z = 0.06$ (where the uniform sample is 10-13 % steeper than the random sample) than at $z = 1$ (where the uniform sample is 1-6 % steeper than the random sample), which can be explained by the relatively smaller range of masses at $z = 1$ than at $z = 0$. This is consistent with Figure 2-4, which show the local relation to be less linear than the $z = 1$ relation. We also note that the precise selection method (uniform in M_{BH} or M_*) is unimportant, with both methods producing equivalent results. Rather it is when the sample is uniformly distributed along the relation that the steeper slope is found.

In addition to the steeper slopes, the mass-selected samples tend to be more sharply peaked than the random sample (the standard deviation of the random sample is roughly double that of the uniformly-selected samples). These narrower peaks are expected, as they have an additional constraint imposed upon the sample selection, providing less possibility for strongly outlying results (e.g. a sub-sample of all low-mass objects [producing a much shallower slope] is possible only in the random sampling). In Table 5 we provide the mean and standard deviation of the distributions for the slope and intrinsic scatter of all three scaling relations using all three sampling methods at redshifts 0.06 and 1. We

confirmed that using smaller sample sizes than 100 (50, and 25) the distributions broaden substantially.

We expect similar behavior in observational samples used to calculate the slope. Observational data tend to be much more heavily weighted toward the massive-end than a random sampling should produce (which should follow the black hole mass function), and are roughly equivalent to our samples uniform in mass. Furthermore, we note that our finding that the high-end of the relation is steeper than the low end is consistent with observations, which have found similar behavior in all three relations (McConnell & Ma 2013). The effect of sample selection could also bias results for redshift evolution unless carefully accounted for. If observational samples at different redshifts have different mass distributions (as is quite likely, due to the difficulty observing small objects at high- z), then the sample more highly-weighted toward the high-end is likely to be steeper, due entirely to the sample selection. We see this explicitly in Table 5, where the $M_{\text{BH}} - \sigma$ ($M_{\text{BH}} - M_*$) relation at $z = 0.06$ is 8, 15, and 17 (2, 9, 11) per cent steeper than at $z = 1$ when using random, uniform- M_{BH} , and uniform- M_* distributions, respectively, despite sampling from the same full population of black holes.

As expected, we note that the sample size has no effect on the mean slope or scatter, and so a small sample size can still reasonably predict the relation (Table 5). Predictably, smaller sample sizes produce a wider distribution regardless of sampling method used, making smaller samples noticeably less reliable: a sample size of 25 results in a 1-sigma uncertainty reaching up to 10% of the slope, and as high as 25-30% of the intrinsic scatter.

4.1 L_{BH} dependence, AGN-luminosity bias

We depend upon the black hole luminosity (L_{BH}) for many observational studies of black holes. Figure 6 shows the local $M_{\text{BH}} - \sigma$ relation, color-coded by several lower-limits on the L_{BH} and the associated power-law fits. There is a clear correlation between a black hole’s mass and luminosity, with brighter black holes tending to be larger mass. This is expected, given that the accretion rate depends on M_{BH}^2 (or M_{BH} , if Eddington limited). However, we note that for a given blackhole mass we tend to find a range of luminosities, as has been previously shown (DeGraf et al. 2012). This range in luminosities means that even when using a luminosity-limited sample, we obtain a similar result to using the full sample. We demonstrate this in Table 3, where the best-fitting parameters for all three scaling relations are listed for cuts on L_{BH} . In all three relations ($M_{\text{BH}} - \sigma$, $M_{\text{BH}} - M_*$, and $M_{\text{BH}} - L_V$) we see the same qualitative behavior: a higher luminosity threshold tends to be slightly larger (higher α), has a steeper dependence on the host (higher β), and a larger intrinsic scatter (larger ϵ_0). However, we note that this dependency is very weak. The normalization (α) only increase by ~ 0.2 dex going from $L_{\text{BH}} > 10^8 L_\odot$ to $> 10^{11} L_\odot$. The slope increase by $\sim 6 - 10\%$ between cuts of $10^8 L_\odot$ and $10^{10} L_\odot$, and although the cut of $10^{11} L_\odot$ may be a bit steeper, the sample size is much smaller with such a high cut (78 objects).

However, when we perform a test based on a faint sample ($L_{\text{BH}} < 10^{11} L_\odot$), a bright sample ($L_{\text{BH}} > 10^{11} L_\odot$), and a subsample of faint black holes matched to the bright

sample according to host stellar mass we find a significant difference. Because the most massive faint black hole is only $10^{9.57} M_\odot$, we only consider BHs below this mass for this sample comparison. With this upper limit on M_{BH} , we find the bright sample slope to be 3.93, and the faint sample slope to be 3.38. To generate the matched sample, for each bright black hole we find the black hole from the faint sample which most closely matches it in host stellar mass (M_*). Repeating this process for 1000 randomized orderings, we find the M_* -matched sample to have a slope of 3.89 ± 0.02 , fully consistent with the bright sample. Thus we find that although the correlations for bright AGNs may appear to be steeper than fainter ones, it is due entirely to the different distribution of host masses that the bright AGN populate. Specifically, bright black holes tend to be more massive black holes and located in larger hosts than fainter ones, but there is no inherent difference between bright and faint AGN of equivalent black hole mass/within equivalent host masses.

Thus there is a bias when black holes are luminosity-selected without any additional considerations, which must be accounted for in flux-limited observations (particularly at high-redshift where the luminosity limits are higher). Any such flux-limited survey must take the M_{BH} distribution into consideration, and should only be compared to measurements from similar M_{BH} -distribution samples (or else recognize that the higher flux limit will bias the result toward a steeper slope). This is particularly important for evolution studies, where a fixed flux limit will bias the high-redshift observations toward a steeper slope unless the mass distribution is accounted for.

Similar to the L_{BH} -dependence, we consider the dependence on AGN-activity. Using a cut on Eddington fraction ($f_{\text{edd}} = \dot{M}_{\text{BH}}/\dot{M}_{\text{edd}}$) as the threshold for activity, we find weak evidence for a dependence on activity at low redshift. At $z = 0.06$, the best fitting $M_{\text{BH}} - \sigma$ slope for BHs with $f_{\text{edd}} > 0.1$ (0.05) is 5.6 (5.0), compared to the full-sample slope of 3.5. As done with the L_{BH} sample, we create a subsample of inactive BHs mass-matched (using M_*) to the active sample, providing slopes of 3.5 ± 1 (3.6 ± 0.7). As $z = 0.3$ we find an active slope of 4.83 (4.1), while the mass-matched inactive samples have slopes of 3.8 ± 1.4 (3.5 ± 0.5) for $f_{\text{edd}} > 0.1$ (0.05), while for $z > 0.3$ we find no difference between the active and inactive populations. Thus we find the local relation is steeper for active black holes, but only slightly outside the 1- σ variation of a comparable inactive sample.

4.2 High-mass sample

To consider the relation for high-mass black holes, in Table 4 we provide the best fitting parameters using only black holes above $10^8 M_\odot$ for $z \leq 2$ (at $z = 4$ we don’t have enough large black holes for an accurate fitting). To confirm that using a strict cut on M_{BH} doesn’t bias our result, we also test using a cut perpendicular to the full relation at $10^8 M_\odot$. The slope and normalization are essentially unaffected (less than 5% difference between selection methods). However, using a strict cut on M_{BH} results in a smaller intrinsic scatter, so we provide the intrinsic scatter for both selection methods.

Compared to the full relation, we find several important differences in the high-mass sample. First, the high-mass sample is generally ~ 0.2 dex higher than the full sam-

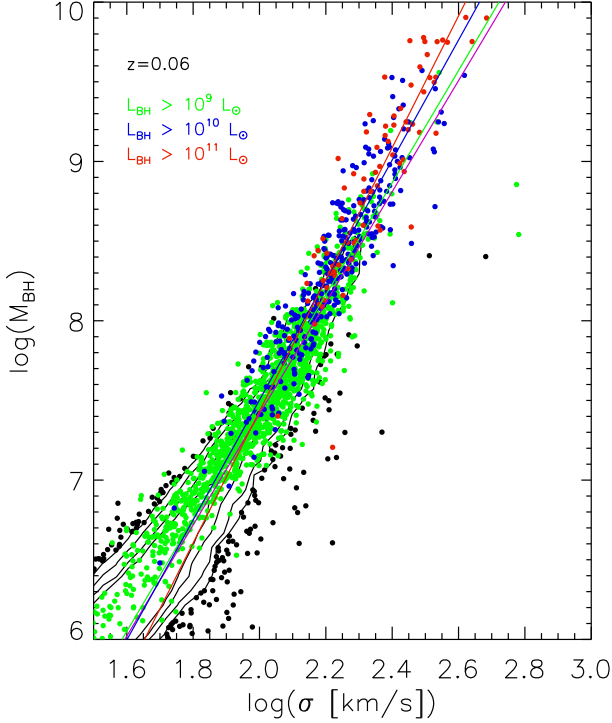


Figure 6. The local $M_{\text{BH}} - \sigma$ relation color-coded by lower-limits on black hole luminosity: Black - all, Green - $> 10^9 L_{\odot}$, Blue - $> 10^{10} L_{\odot}$, Red - $> 10^{11} L_{\odot}$.

ple, suggesting that massive black holes tend to be about 50% larger relative to their host galaxy than low-mass black holes. At low redshift we find a larger intrinsic scatter among the high-mass sample, due in large part to the strongly undermassive outliers at low- z . At higher redshift (redshift above ~ 1) the trend reverses, with the high-mass sample (where we have fewer outliers) having a smaller scatter than the full relation. This can also be seen in Figures 2-4, where the largest scatter in the relation tends to be at moderate masses.

Most significantly, however, we find the high-mass slope to be shallower than that of the full sample (consistent with Volonteri & Stark 2011), and the discrepancy becomes more significant at higher redshift. At $z = 1$, the high mass samples are 20%, 29%, and 53% steeper than the full sample for $M_{\text{BH}} - \sigma$, $M_{\text{BH}} - M_*$, and $M_{\text{BH}} - L_V$, respectively. This shallower slope at high mass suggests that once black holes reach a sufficiently high mass, they begin growing slower relative to their host galaxy, fully consistent with previous work which found that high-mass black holes tend to grow slower than moderate mass black holes (DeGraf et al. 2012). This behavior is investigated in more detail in Section 5. The shallower slope is also very important for high-redshift observations, which are generally only able to constrain the properties of high-mass black holes and thus might underestimate the slope of the full sample if the selection function is not properly accounted for.

Parameters for relation using high-mass sample			
z	α	β	ϵ_0
$M_{\text{BH}} - \sigma$ relation ($x_0 = 200 \text{ km/s}$)			
0.06	8.582 ± 0.011	3.270 ± 0.094	0.225 (0.221)
0.3	8.434 ± 0.010	3.073 ± 0.093	0.189 (0.190)
0.6	8.327 ± 0.010	2.812 ± 0.092	0.182 (0.180)
1	8.285 ± 0.009	2.706 ± 0.087	0.166 (0.183)
2	8.301 ± 0.012	2.315 ± 0.125	0.178 (0.184)
$M_{\text{BH}} - M_*$ relation ($x_0 = 10^{11} M_{\odot}$)			
0.06	8.122 ± 0.015	1.102 ± 0.032	0.239 (0.249)
0.3	8.073 ± 0.014	1.039 ± 0.030	0.191 (0.207)
0.6	8.046 ± 0.013	0.978 ± 0.030	0.182 (0.191)
1	8.080 ± 0.013	0.942 ± 0.031	0.176 (0.197)
2	8.250 ± 0.013	0.843 ± 0.043	0.180 (0.217)
$M_{\text{BH}} - L_V$ relation ($x_0 = 10^{10.5} L_{\odot}$)			
0.06	8.468 ± 0.014	0.825 ± 0.036	0.308 (0.354)
0.3	8.389 ± 0.011	0.848 ± 0.033	0.237 (0.283)
0.6	8.287 ± 0.011	0.793 ± 0.033	0.221 (0.247)
1	8.185 ± 0.013	0.782 ± 0.035	0.215 (0.254)
2	8.117 ± 0.021	0.625 ± 0.043	0.212 (0.259)

Table 4. Best fitting parameters for the scaling relations (Equation 1) based on a sample of black holes with $M_{\text{BH}} > 10^8 M_{\odot}$. We also provide ϵ_0 for a cut perpendicular to the full relation in parentheses (see text).

4.3 Intrinsic scatter

Having found the best fitting functions for the main scaling relations, we also investigate the distribution of black holes about this relation. In Figure 7 we plot the distribution function of $\Delta \log(M_{\text{BH}})$, the offset of the black hole mass from each of the best-fitting scaling relations (solid histograms: black - $M_{\text{BH}} - \sigma$; red - $M_{\text{BH}} - M_*$; blue - $M_{\text{BH}} - L_V$) at redshift zero. We find that the scatter in the scaling relations tends to be well fit by Gaussian distributions, showing the distribution is generally symmetric about the mean relation (except for low-end outliers, discussed below, and in Section 4.4). For each relation, we overplot the Gaussian with standard deviation equal to the intrinsic scatter found in Section 3. The good agreement shows that the distribution of black holes about the best fitting relation is indeed Gaussian, and that the intrinsic scatter ϵ_0 can be well-calculated as in Section 3.1. The Gaussian nature of the scatter in each of the scaling planes is particularly important for observational studies, where knowledge of the underlying scatter is needed for creating a selection function.

In Figure 8 we show the distribution of black hole offsets based on the $M_{\text{BH}} - M_*$ relation, binned by host stellar mass. For low- to moderate-stellar mass, the distribution is roughly M_* -independent. At the highest masses ($M_* > 10^{11.5} M_{\odot}$), however, the distribution is shifted upward, such that the black holes tend to lie above the relation by ~ 0.1 dex, with a larger high-end tail to the distribution. We also find that the majority of the significantly undermassive objects (at least 1 dex below mean relation) tend to be found in these very high-mass hosts, and can be identified as they are strong outliers from the otherwise Gaussian distribution.

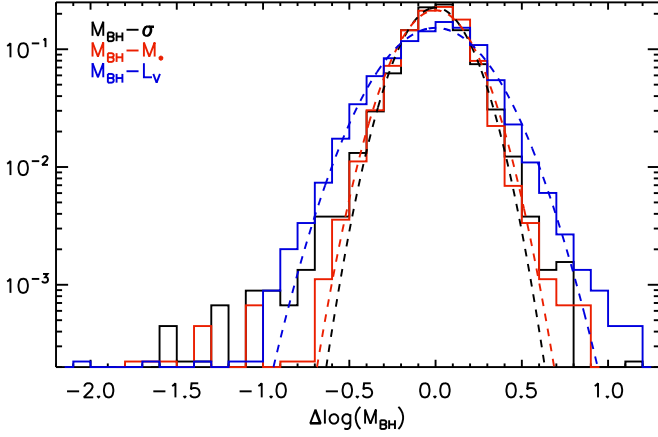


Figure 7. Distribution of black hole offset relative to the best fitting scaling relations provided in Table 2: *Black*: M_{BH} offset relative to $M_{\text{BH}}-\sigma$ relation *Red*: M_{BH} offset relative to $M_{\text{BH}}-M_*$ relation *Blue*: M_{BH} offset relative to $M_{\text{BH}}-L_V$ relation. Dashed lines show the best-fitting Gaussian distributions.

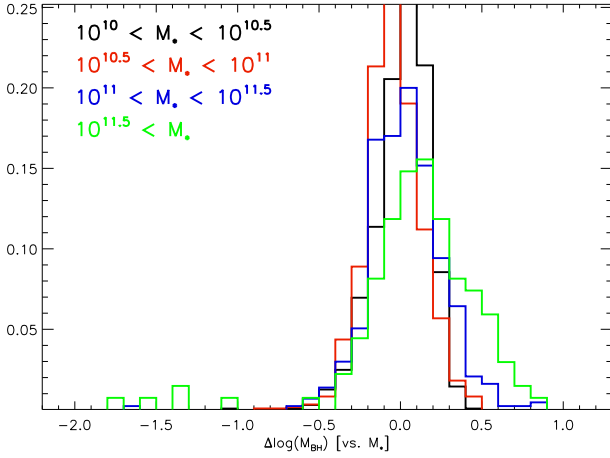


Figure 8. Distribution of black hole offset relative to $M_{\text{BH}}-M_*$ relation at $z = 0.06$, binned by host stellar mass. *Black* - $10^{10} < M_* < 10^{10.5}$, *Red* - $10^{10.5} < M_* < 10^{11}$, *Blue* - $10^{11} < M_* < 10^{11.5}$, *Green* - $10^{11.5} < M_*$.

4.4 Outliers

As mentioned in Section 4, the distributions in Figures 9 and 10 are based on samples which neglect the strongest outliers, identifiable as being well outside the otherwise Gaussian scatter about the mean relation (Section 4.3). Including those outliers has minimal effect on the random distribution (since they are so rarely selected), however the uniform distributions include them much more frequently, resulting in bimodal distributions. We show this in Figures 9 and 10 with a pink curve, which uses uniform samples in M_{BH} based on all BHs (i.e. equivalent to the green curve except with the outliers included). In the $M_{\text{BH}}-L_V$ relation, the inclusion of these objects has minimal effect, since that relation's larger intrinsic scatter means they are much weaker outliers. In the $M_{\text{BH}}-\sigma$ and $M_{\text{BH}}-M_*$ relations, however, we can see

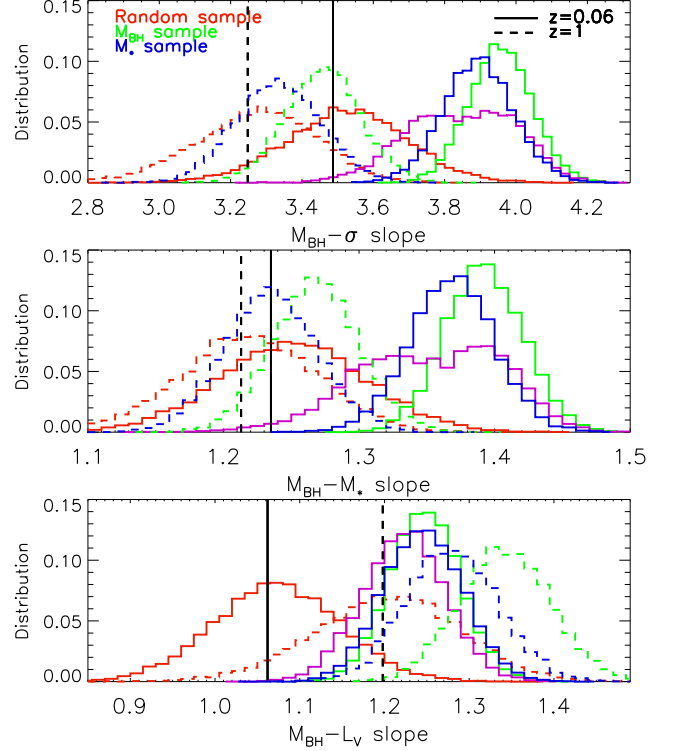


Figure 9. The probability distribution function of the best fit slopes of $M_{\text{BH}}-\sigma$ (top), $M_{\text{BH}}-M_*$ (middle), and $M_{\text{BH}}-L_V$ (bottom) using subsamples of 100 objects from our full population at $z = 0.06$ (solid lines) and $z = 1$ (dashed lines). The sampling techniques are a random sampling (red), a sample uniformly distributed in M_{BH} (green), and a sample uniformly distributed in M_* (blue). Each distribution is found using 10,000 distinct samplings, after removing the four strongest outliers from the $z = 0$ population (see text). In pink we show the distribution of the M_{BH} -selected sample if those outliers are not removed. We also show the best fit slope from the full population as vertical lines.

a strong change when including these outliers, resulting in a much broader distribution of slopes (standard deviation of 0.15 compared to 0.09 when the outliers are removed) and a clear bimodality in the distribution of intrinsic scatter (samples without any outliers have $\epsilon_0 \sim 0.19$ compared to $\epsilon_0 \sim 0.25$ for samples which include an outlier).

When fitting these subsamples, we found an interesting bimodality arising from the four outlying points seen in the $z = 0$ panel of Figure 3. In these smaller samples, the inclusion of one of these outlying points had a significant effect on the slope and especially the intrinsic scatter, producing a wide distribution of slopes and a clearly bimodal distribution of the scatter. To avoid such strong contamination from only a few objects, we remove those four outliers and re-calculate the fits, resulting in the elimination of the bimodality. We note that the size of the secondary peak caused by the inclusion of at least one outlier is strongly dependent on the sample size used. Smaller sample sizes have a smaller secondary peak (since it is less likely to capture one of the outliers), but the secondary peak moves further from the primary peak (since the effect of the outlier is larger in a smaller sample).

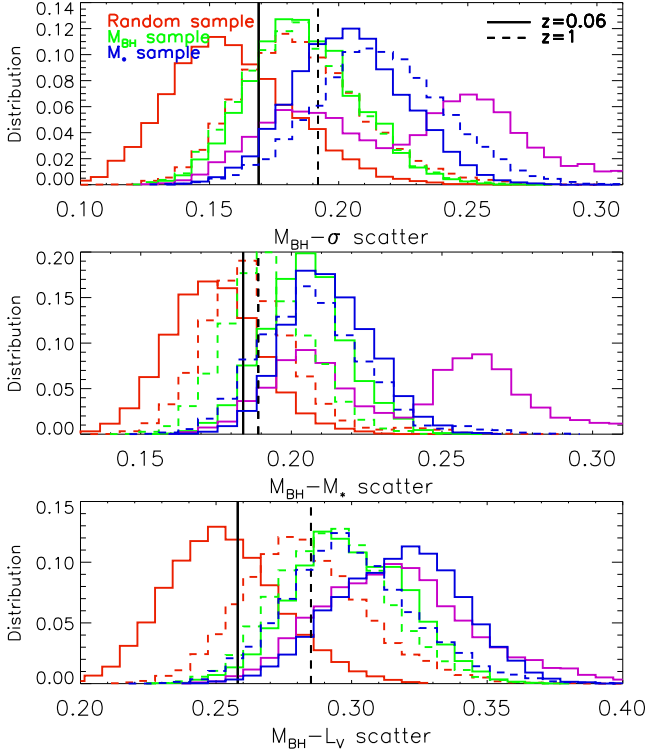


Figure 10. As Figure 9 but for the intrinsic scatter (ϵ_0) rather than the slope.

Distribution of fitted parameters					
z	Selection method	$\langle \beta \rangle$	$\sigma(\beta)$	$\langle \epsilon_0 \rangle$	$\sigma(\epsilon_0)$
$M_{\text{BH}} - \sigma$					
0.06	Random	3.52	0.17	0.16	0.02
	Uniform M_{BH}	3.96	0.09	0.19	0.02
	Uniform M_*	3.89	0.10	0.20	0.02
1	Random	3.27	0.17	0.19	0.02
	Uniform M_{BH}	3.46	0.11	0.19	0.02
	Uniform M_*	3.33	0.12	0.22	0.03
$M_{\text{BH}} - M_*$					
0.06	Random	1.25	0.06	0.17	0.02
	Uniform M_{BH}	1.39	0.03	0.20	0.01
	Uniform M_*	1.37	0.03	0.21	0.01
1	Random	1.22	0.05	0.19	0.02
	Uniform M_{BH}	1.27	0.03	0.19	0.01
	Uniform M_*	1.23	0.03	0.21	0.02
$M_{\text{BH}} - L_V$					
0.06	Random	1.07	0.07	0.25	0.02
	Uniform M_{BH}	1.25	0.04	0.30	0.02
	Uniform M_*	1.25	0.05	0.32	0.02
1	Random	1.20	0.09	0.28	0.02
	Uniform M_{BH}	1.34	0.05	0.29	0.02
	Uniform M_*	1.28	0.05	0.30	0.02

Table 5. Mean and standard deviation of slope (β) and intrinsic scatter (ϵ_0) for subsamples of 100 objects selected at random, or with uniform distributions in M_{BH} or M_* (see text for details).

5 EVOLUTION OF BH HOLES ON THE $M_{\text{BH}} - M_*$ PLANE

In Figure 11 we show the $M_{\text{BH}} - M_*$ relation at $z = 0.6$, with each black hole color-coded by the slope of its evolution along the $M_{\text{BH}} - M_*$ plane from $z = 0.6$ to $z = 0.06$. Green points show black holes which evolve along a shallower slope than the best fit local relation (i.e. black holes which are becoming less massive relative to their host). Blue points show black holes which are steeper than the local relation (i.e. black holes which are becoming more massive relative to their host). The red points are cases in which the slope is negative, due to the stellar mass of the host decreasing from $z = 0.6$ to $z = 0.06$. Ignoring the rare cases where the host galaxy has gotten smaller, we find a clear trend in the slopes displayed here. Black holes which are overmassive for their given host mass tend to grow slower than their host (i.e. shallower slope than the local relation, so blue points), bringing them toward the local relation. In contrast, the undermassive black holes tend to grow more rapidly, bringing them up toward (and often above) the relation.

This is shown statistically in Figure 12, which plots the correlation between ΔM_{BH} (i.e. how overmassive the black hole is relative to the host stellar mass) and the slope of the black holes trajectory along the $M_{\text{BH}} - M_*$ plane from $z = 0.3$ to 0.06 . Here we clearly see that the more overmassive the black hole, the shallower its trajectory along the scaling relation. Overmassive black holes ($\Delta \log(M_{\text{BH}}) > 0$) are much more likely to move on a shallow trajectory, with 86% having a shallower trajectory than the slope of the local relation. 49% of undermassive black holes have a shallower trajectory, falling to 28% for black holes undermassive by at least 0.3 dex. The best fit relation between the slope trajectory and $\Delta \log(M_{\text{BH}})$ is $1.08 \times (\Delta \log(M_{\text{BH}}))^{-0.46}$. This is consistent with our general picture for how black holes evolve with respect to their galaxies: low-mass black holes tend to grow quickly, bringing them up and often above the local relation; upon reaching a sufficiently large mass (i.e. above the relation), the black hole enters a self-regulated regime, suppressing its further growth while the host continues to grow, bringing it back to the general relation we find. This is also supported by the M_{BH} -dependence of the relation (Table 4), which found the high-mass black holes (which tend to be overmassive and in the self-regulated regime) have a shallower slope than lower-mass objects. We note that Volonteri & Natarajan (2009) find similar behavior for low-mass black hole growth fueled by galaxy mergers, where black holes seeded below the relation tend to grow rapidly without significant self-regulation, while the more massive objects tend to have minimal growth until the host halo has grown significantly.

To determine if the trajectory a black hole takes along the scaling relation is a function of its activity, in Figure 13 we show a histogram of the Eddington fraction of the black holes at $z = 0.06$ (top) and 0.3 (bottom), divided into two populations: one for black holes whose path on the $M_{\text{BH}} - M_*$ plane is steeper than the local relation (black) and one for those whose path is shallower (red). We find that there is minimal difference between the two distributions, suggesting that the path taken along the scaling plane is not strongly dependent on the black holes' Eddington fraction. However, we note that this is based upon the slope for a single step

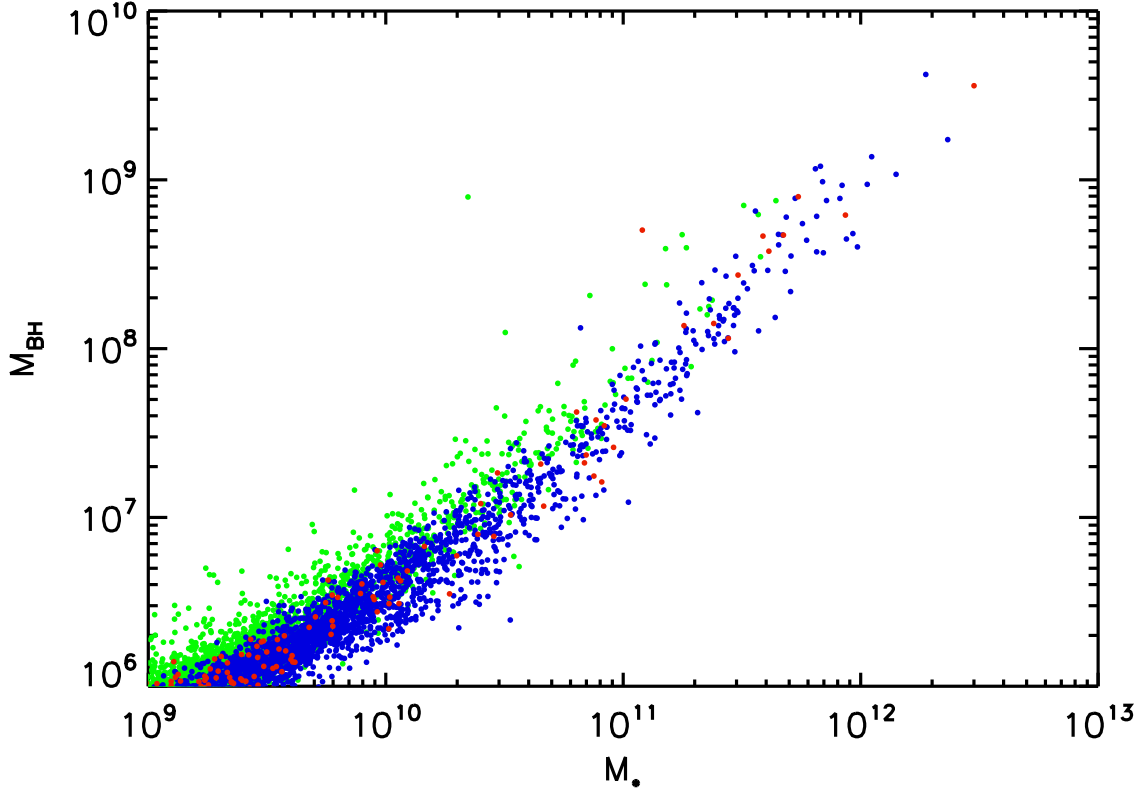


Figure 11. $M_{\text{BH}} - M_*$ plot at $z = 0.6$, color-coded by individual black hole evolution along the $M_{\text{BH}} - M_*$ plane. The BH population is divided into three categories based on evolution from $z = 0.6$ to $z = 0.06$: Green - slope along $M_{\text{BH}} - M_*$ plane is positive, but shallower than the local relation; Blue - slope is positive, and steeper than the local relation; Red - slope is negative (i.e. rare case where M_* has decreased). To avoid spurious slopes from small evolution, only objects with a change of at least 30% in both M_{BH} and M_* are included.

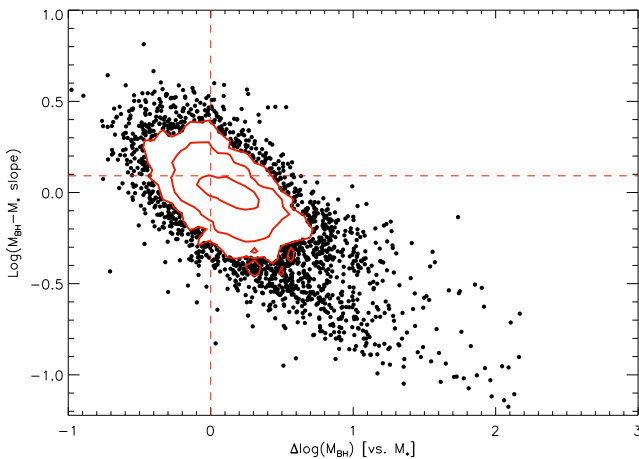


Figure 12. Correlation between the black hole offset relative to the local $M_{\text{BH}} - M_*$ relation ($\Delta \log(M_{\text{BH}})$) and the slope of its trajectory along the $M_{\text{BH}} - M_*$ plane. The vertical dashed line is the threshold for lying on the local $M_{\text{BH}} - M_*$ plane, and the horizontal dashed line is the slope of the local relation.

from $z = 0.3$ to $z = 0.06$, while the accretion rate of the black hole (and thus the Eddington fraction) varies on much shorter timescales. To fully characterize the correlation (if any) between AGN activity and motion along the scaling

plane will require an investigation into the co-evolution of BH and host galaxy with much finer time resolution, which we leave for a future work.

To explicitly illustrate black hole evolution along the scaling relations, in Figure 14 we show the $M_{\text{BH}} - \sigma$ and $M_{\text{BH}} - M_*$ planes at $z = 0.06$, with the tracks of two black holes overplotted on top in green, and the local relation shown in pink. These two tracks show the typical behavior described here. In each case, the black hole grows along a trajectory steeper than the local relation, bringing it up to the local relation (similar to Volonteri & Natarajan 2009). This continues until the end of the simulation for the more massive BH, without reaching a regulated regime (but also without rising above the local relation). The second BH, however, does reach a self-regulated regime. In the $M_{\text{BH}} - \sigma$ plane it only barely surpasses the local relation, but it more strongly overcomes it in the $M_{\text{BH}} - M_*$ plane. At this point the black hole growth slows substantially, while the host continues growing (in both σ and M_*), bringing the black hole under the local relation. Once below the local relation, the host galaxy undergoes a merger. This merger is sufficient to restart the black hole growth, bringing the black hole back to slightly above the local relation.

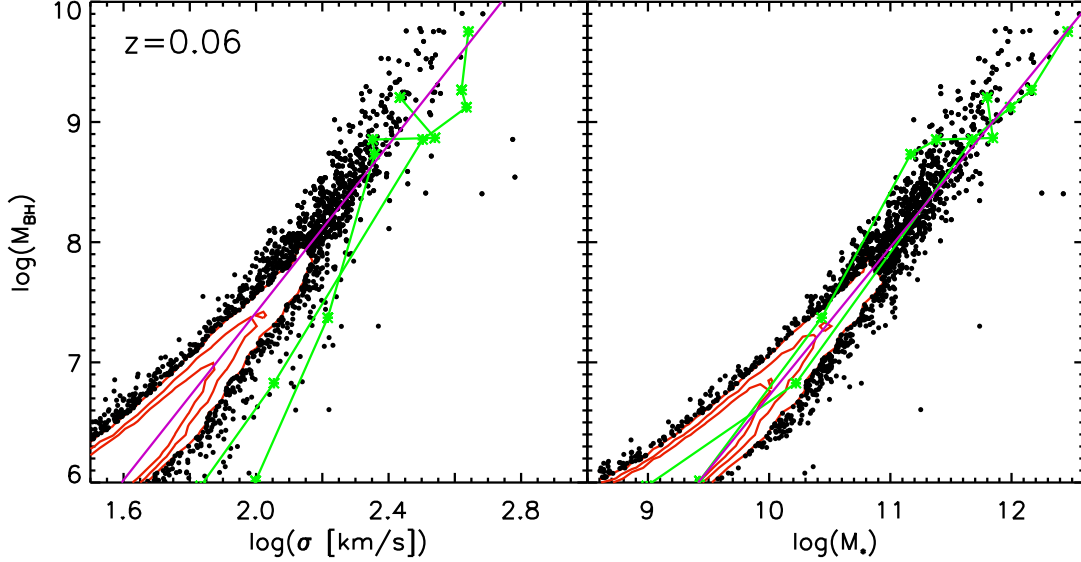


Figure 14. The $M_{\text{BH}} - \sigma$ and $M_{\text{BH}} - M_*$ (right) relations at $z = 0.06$, with tracks from two individual black holes shown in green. These tracks show the evolution of each object over their lifespan, until reaching their final location at the end of the simulation.

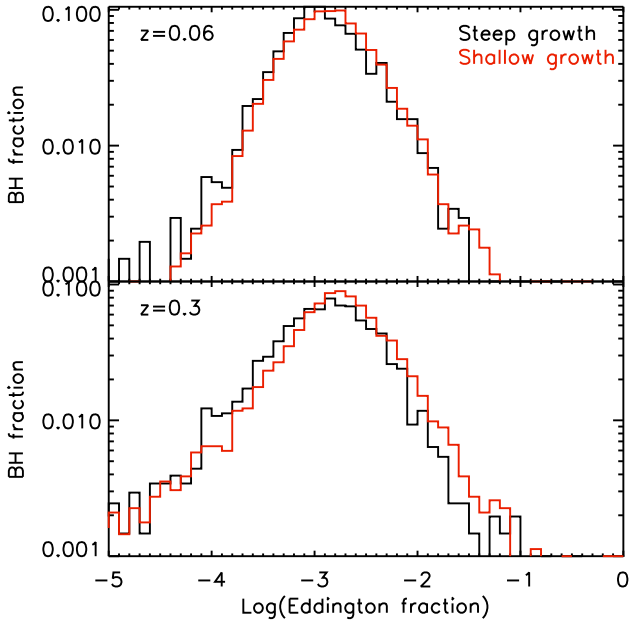


Figure 13. Distribution of the Eddington fraction ($\dot{L}_{\text{BH}}/\dot{L}_{\text{edd}}$) at $z = 0.06$ (top) and $z = 0.3$ (bottom) for black holes whose evolution along the $M_{\text{BH}} - M_*$ plane steeper (black) or shallower (red) than the slope of the local relation.

6 CONCLUSIONS

We have presented the scaling relation between supermassive black holes and their host galaxies from the high-resolution cosmological simulation *MassiveBlackII*. The volume of this simulation provides a large sample size of black holes reaches $\sim 10^{10} M_{\odot}$ by $z \sim 0$, which we use to study the scaling relations across a wide range of redshifts, considering both how the relation evolves with cosmic time, and how individual black holes tend to evolve relative to the relation.

The simulation does a good job reproducing all three major scaling relations investigated: $M_{\text{BH}} - \sigma$, $M_{\text{BH}} - M_*$, and $M_{\text{BH}} - L_V$. In the $M_{\text{BH}} - \sigma$ relation, we match the high-end data very closely. The low-end of our results tend to lie above the observations, but given the much closer agreement in the relations with M_* and L_V , we expect this to be primarily due to the computation of σ rather than an overestimate in the black hole mass. This is consistent with Sijacki et al. (2014), who found similar behavior at the low-end, at least in part due to the contributions from a non-negligible rotational component to σ . This will be addressed in a future work on the full bulge-decomposition of galaxies within the simulation.

The $M_{\text{BH}} - M_*$ and $M_{\text{BH}} - L_V$ relations, both based on the total galaxy rather than bulge properties, also show good agreement at the high end, as well as closer agreement at the low-end of the relation, particularly in M_* , the more fundamental of the two properties within our simulation. The $M_{\text{BH}} - L_V$ relation has the largest scatter among the three relations investigated, suggesting it to be a less fundamental relation than either of the other two. This lesser correlation is not surprising, given that the stellar mass is a more fundamental quantity during the run, and the velocity dispersion is more directly related to the potential well of the host. The low-end $M_{\text{BH}} - L_V$ relation tends to flatten out at high- z as the black hole seed mass is approached, showing a clear break in the relation. However, this is in the least well-resolved objects (both quite small and quite young), and given that the break disappears after $z \sim 2$ and isn't found in either σ or M_* , we expect this is likely an artifact of the simulation.

Within each of the three scaling relations, we test the scatter of black holes above and below the local relation, and find it to be well-described by a Gaussian distribution (with standard deviation equal to the intrinsic scatter ϵ_0 in Table 2), except in the highest mass hosts. In the largest host galaxies ($M_* > 10^{11.5} M_{\odot}$) the scatter is biased toward larger (by ~ 0.1 dex) black holes, with a stronger high-end

tail to the distribution. Thus we suggest that observations should not assume a Gaussian spread in the selection function among high-mass objects.

We consider the evolution of the relation with redshift, and find none of the three relations exhibit strong evolution for $z \leq 1$. Above redshift 1, black holes of a given mass tend to be found in higher- σ , lower- L_V hosts. This evolution is found to be mass-dependent, with massive black holes being found in slightly less-massive hosts (shown explicitly as a mass-offset relative to the local relation). This is consistent with previous findings that massive black hole growth is more rapid at high-redshifts (DeGraf et al. 2012).

In contrast to the offset evolution based on M_* , the offset relative to L_V decreases with time, suggesting the black holes of a given mass tend to be found in brighter hosts at high- z . This evolution is due primarily to the evolution of the mass-to-light ratio (with high- z galaxies tending to be brighter than their low- z counterparts), rather than an evolution in the BH-host relation. This is clearly seen when compared to the $M_{\text{BH}} - M_*$ relation, which shows the opposite trend, or when considering the correlation between M_{BH} and $L_{V,0}$, i.e. the luminosity corrected for passive evolution. To compare directly with observations, we consider the evolution in offset based on the $M_{\text{BH}} - L_{V,0}$ local relation using only black holes with $M_{\text{BH}} > 10^8 M_\odot$ and $z \leq 0.6$, finding a relation of $M_{\text{BH}}/L_{V,0} \propto (1+z)^{1.0 \pm 0.1}$. This is fully consistent with the current observational measurement of $M_{\text{BH}}/L_{\text{host},0} \propto (1+z)^{1.2 \pm 0.7}$ (Park et al. 2014, private correspondence).

When considering cuts on the black hole luminosity, we find all three relations to be nearly completely L_{BH} -independent. From a theoretical standpoint, this is significant as it demonstrates that black holes in any given region of the BH-host plane can span a wide range of accretion rates (though with a general trend of larger black holes tending to be brighter). In other words, we expect any given set of $M_{\text{BH}} - \sigma, M_*, L_V$ values to include some black holes accreting at unusually high eddington fractions, while others will be at unusually low fractions. From an observational standpoint, this is significant since it means that for any given survey, the flux limit imposed by the instrumentation will limit only the sample size that can be measured and the range over which the sample will span; the flux limits will *not* result in a bias for the detected slope of the relation being studied, which will be of crucial importance for upcoming high-redshift surveys.

In addition we consider the relation of only the high-mass black holes, finding they tend to be ~ 0.2 dex larger relative to their host. However, the high-mass sample has a shallower slope, suggesting that the highest-mass black holes grow slower (relative to their host galaxy) than more moderate mass objects. We investigate this in more detail by considering the behavior of individual black holes and their evolution along the BH-host planes. In general, we find that black holes tend to evolve toward the local relation, resulting in a general decrease in the intrinsic scatter within the relation. Black holes below the local relation tend to grow more rapidly, bringing them up toward (and even above) the general relation. Once grown to be ‘overmassive’ relative to the relation, a self-regulated regime may be entered, suppressing further black hole growth without necessarily inhibiting host growth. This results in a much shallower evolution along the

plane, bringing the overmassive black hole back toward the mean relation. Thus we generalize the black hole behavior as initial rapid growth, suppressed only upon surpassing the mean relation, at which point regulation of the black hole growth brings it back toward the typical relation.

Finally, we consider the effect sampling has on the scaling relation. We find that truly random sampling is equivalent to the full population, though with substantial spread in the distribution, especially for smaller sample sizes (e.g. standard deviation in the $M_{\text{BH}} - \sigma$ slope is ~ 0.17 for a sample of 100, and ~ 0.35 for a sample of 25). However, both the full population and the random sub-samples tend to be dominated by the low end (since the low-mass objects drastically outnumber the massive ones). In contrast to this, a sample with a uniform distribution of masses (either M_{BH} or M_*) will not be affected this way. By probing all scales equally, the result is less biased toward the typically shallower low-end, producing a much steeper result. Furthermore, the distribution of slopes tends to have a narrower distribution, since the uniform distribution in mass makes a biased subsample much less likely. We also note that distributions which uniformly span the mass range considered tend to find a stronger redshift evolution than a random sampling of objects does. Since the high-mass objects tend to evolve more quickly, the sampling which weights the high-end more strongly (the uniform distribution) will necessarily find a quicker evolution than one which weights the low-end more strongly (the full population and the random sampling). This possible bias toward redshift-evolution of the slope of the relations must be carefully addressed in any high-redshift observational study.

ACKNOWLEDGMENTS

The simulations were run on NSF XSEDE facilities (Kraken at the National Institute for Computational Sciences). We acknowledge support from Moore foundation which enabled us to perform the simulations and data analysis at the McWilliams Center of Cosmology at Carnegie Mellon University. TDM has been funded by the National Science Foundation (NSF) PetaApps, OCI-0749212 and by NSF AST-1009781 and ACI-1036211. TT acknowledges support from the Packard Foundation through a Packard Research Fellowship, from NASA through grants HST-AR-12625, GO-10216, GO-11208, GO-11166. We thank Matthew Auger and Vardha Bennert for comments and discussion.

REFERENCES

- Bachmann L. K., Dolag K., Hirschmann M., Almodena Prieto M., Remus R.-S., 2014, ArXiv e-prints
- Begelman M. C., Volonteri M., Rees M. J., 2006, MNRAS, 370, 289
- Bennert V. N., Auger M. W., Treu T., Woo J.-H., Malkan M. A., 2011a, ApJ, 726, 59
- Bennert V. N., Auger M. W., Treu T., Woo J.-H., Malkan M. A., 2011b, ApJ, 742, 107
- Bennert V. N., Treu T., Woo J.-H., Malkan M. A., Le Bris A., Auger M. W., Gallagher S., Blandford R. D., 2010, ApJ, 708, 1507

- Bondi H., 1952, *MNRAS*, 112, 195
- Bondi H., Hoyle F., 1944, *MNRAS*, 104, 273
- Booth C. M., Schaye J., 2009, *MNRAS*, 398, 53
- Bower R. G., Benson A. J., Malbon R., Helly J. C., Frenk C. S., Baugh C. M., Cole S., Lacey C. G., 2006, *MNRAS*, 370, 645
- Bromm V., Larson R. B., 2004, *ARA&A*, 42, 79
- Bromm V., Loeb A., 2003, *ApJ*, 596, 34
- Ciotti L., Ostriker J. P., Proga D., 2009, *ApJ*, 699, 89
- Colberg J. M., di Matteo T., 2008, *MNRAS*, 387, 1163
- Croft R. A. C., Di Matteo T., Springel V., Hernquist L., 2009, *MNRAS*, 400, 43
- Croton D. J., et al., 2006, *MNRAS*, 365, 11
- DeGraf C., Di Matteo T., Khandai N., Croft R., 2012, *ArXiv e-prints*
- DeGraf C., Di Matteo T., Springel V., 2010, *MNRAS*, 402, 1927
- Degraf C., Di Matteo T., Springel V., 2011, *MNRAS*, 413, 1383
- Di Matteo T., Colberg J., Springel V., Hernquist L., Sijacki D., 2008, *ApJ*, 676, 33
- Di Matteo T., Khandai N., DeGraf C., Feng Y., Croft R. A. C., Lopez J., Springel V., 2012, *ApJL*, 745, L29
- Di Matteo T., Springel V., Hernquist L., 2005, *Nature*, 433, 604
- Escala A., Larson R. B., Coppi P. S., Mardones D., 2004, *ApJ*, 607, 765
- Fanidakis N., Baugh C. M., Benson A. J., Bower R. G., Cole S., Done C., Frenk C. S., 2011, *MNRAS*, 410, 53
- Ferrarese L., 2002, *ApJ*, 578, 90
- Fioc M., Rocca-Volmerange B., 1997, *A&A*, 326, 950
- Fioc M., Rocca-Volmerange B., 1999, *ArXiv Astrophysics e-prints*
- Gebhardt K., et al., 2000, *ApJL*, 539, L13
- Graham A. W., Erwin P., Caon N., Trujillo I., 2001, *ApJL*, 563, L11
- Gültekin K., et al., 2009, *ApJ*, 698, 198
- Häring N., Rix H.-W., 2004, *ApJL*, 604, L89
- Hirschmann M., Dolag K., Saro A., Bachmann L., Borgani S., Burkert A., 2014, *MNRAS*, 442, 2304
- Hoyle F., Lyttleton R. A., 1939, in *Proceedings of the Cambridge Philosophical Society*, vol. 35 of *Proceedings of the Cambridge Philosophical Society*, 405
- Johansson P. H., Naab T., Burkert A., 2008, *Astronomische Nachrichten*, 329, 956
- Khandai N., Di Matteo T., Croft R., Wilkins S. M., Feng Y., Tucker E., DeGraf C., Liu M.-S., 2014, *ArXiv e-prints*
- Kormendy J., Ho L. C., 2013, *ARA&A*, 51, 511
- Lauer T. R., Tremaine S., Richstone D., Faber S. M., 2007, *ApJ*, 670, 249
- Lemson G., Virgo Consortium t., 2006, *ArXiv Astrophysics e-prints*: 0608019
- Lopez J., Degraf C., DiMatteo T., Fu B., Fink E., Gibson G., 2011, in *Statistical and Scientific Databases Management Conference (SSDBM)*, Portland, OR
- Magorrian J., et al., 1998, *AJ*, 115, 2285
- Makino J., Funato Y., 2004, *ApJ*, 602, 93
- Mayer L., Kazantzidis S., Madau P., Colpi M., Quinn T., Wadsley J., 2007, *Science*, 316, 1874
- McConnell N. J., Ma C.-P., 2013, *ApJ*, 764, 184
- McConnell N. J., Ma C.-P., Gebhardt K., Wright S. A., Murphy J. D., Lauer T. R., Graham J. R., Richstone D. O., 2011, *Nature*, 480, 215
- Merloni A., et al., 2010, *ApJ*, 708, 137
- Park D., Woo J.-H., Bennert V. N., Treu T., Auger M. W., Malkan M. A., 2014, *ArXiv e-prints*
- Ragone-Figueroa C., Granato G. L., Murante G., Borgani S., Cui W., 2013, *MNRAS*, 436, 1750
- Schulze A., Wisotzki L., 2011, *A&A*, 535, A87
- Schulze A., Wisotzki L., 2014, *MNRAS*, 438, 3422
- Shakura N. I., Sunyaev R. A., 1973, *A&A*, 24, 337
- Sijacki D., Springel V., di Matteo T., Hernquist L., 2007, *MNRAS*, 380, 877
- Sijacki D., Springel V., Haehnelt M. G., 2009, *MNRAS*, 400, 100
- Sijacki D., Vogelsberger M., Genel S., Springel V., Torrey P., Snyder G., Nelson D., Hernquist L., 2014, *ArXiv e-prints*
- Silk J., Rees M. J., 1998, *A&A*, 331, L1
- Springel V., 2005, *MNRAS*, 364, 1105
- Springel V., Hernquist L., 2003, *MNRAS*, 339, 289
- Springel V., et al., 2005, *Nature*, 435, 629
- Tenneti A. e. a., 2014, in *prep*
- Tremaine S., et al., 2002, *ApJ*, 574, 740
- Treu T., Woo J.-H., Malkan M. A., Blandford R. D., 2007, *ApJ*, 667, 117
- Vogelsberger M., et al., 2014, *MNRAS*, 444, 1518
- Volonteri M., Natarajan P., 2009, *MNRAS*, 400, 1911
- Volonteri M., Rees M. J., 2006, *ApJ*, 650, 669
- Volonteri M., Stark D. P., 2011, *MNRAS*, 417, 2085
- Wandel A., Peterson B. M., Malkan M. A., 1999, *ApJ*, 526, 579
- Williams M. J., Bureau M., Cappellari M., 2010, *MNRAS*, 409, 1330
- Woo J.-H., Treu T., Malkan M. A., Blandford R. D., 2006, *ApJ*, 645, 900
- Woo J.-H., Treu T., Malkan M. A., Blandford R. D., 2008, *ApJ*, 681, 925
- Yoshida N., Omukai K., Hernquist L., Abel T., 2006, *ApJ*, 652, 6